

The distance and properties of hydrogen clouds in the Leading Arm of the Magellanic System

B.-Q. For,^{1★} L. Staveley-Smith,^{1★} N. M. McClure-Griffiths,^{2★} T. Westmeier¹
and K. Bekki¹

¹ICRAR, University of Western Australia, Crawley, WA 6009, Australia

²Research School of Astronomy & Astrophysics, Australian National University, Canberra, ACT 2611, Australia

Accepted 2016 June 3. Received 2016 May 31; in original form 2016 April 6

ABSTRACT

We present a high-resolution study of five high-velocity clouds in the Magellanic Leading Arm region. This is a follow-up study of our widefield Parkes survey of the region in order to probe the multiphase structures of the clouds and to give an insight to their origin, evolution and distance. High-resolution data were obtained from the Australia Telescope Compact Array. By combining with single-dish data from the Galactic All-Sky Survey, we are able to probe compact and diffuse emission simultaneously. We identify resolved and unresolved clumps. Physical parameters were derived for both diffuse structure and compact clumps. The latter are cold with typical velocity linewidths of 5 km s^{-1} . We find a gradient in thermal halo pressure, hydrogen density and H I column density of high-velocity clouds as a function of Galactic latitude. This is possibly the first observational evidence of varying distance in the Leading Arm region, with the leading part of the Leading Arm (LA II and III) probably being closer to the Galactic disc than the trailing end (LA I).

Key words: ISM: clouds – ISM: kinematics and dynamics – ISM: structure – radio lines: ISM.

1 INTRODUCTION

High-velocity clouds (HVCs; Muller, Oort & Raimond 1963) are neutral atomic hydrogen gas clouds distributed across the entire sky as large, homogeneous complexes, and include the Magellanic Stream (MS; Mathewson, Cleary & Murray 1974), as well as numerous compact and isolated clouds. They are characterized by a high radial velocity that is forbidden by a simple Galactic rotation model. To classify HVCs, Wakker (1991) introduced the so-called ‘deviation velocity’, which is defined as the smallest difference between the velocity of the cloud and that of the Galactic disc gas along the line-of-sight, and suggested a deviation velocity of at least 50 km s^{-1} for HVCs.

The origin of HVCs has been under debate for decades. A hypothesis of an extragalactic origin was put forward by Blitz et al. (1999). They argued that the observed properties of HVCs are consistent with a distribution across the entire Local Group. In fact, numerical simulations by Klypin et al. (1999) and Moore et al. (1999) suggested that HVCs, excluding some of the large HVC complexes and the MS, might even be the missing dark matter satellites as predicted by cosmological dark matter models. Braun & Burton (1999) conducted a study using the Leiden/Dwingeloo Survey of Galactic neu-

tral hydrogen (LDS; Hartmann & Burton 1997). They identified a subclass of HVCs, namely compact high-velocity clouds (CHVCs), which are isolated, have an angular diameter of $\leq 2^\circ$ and H I column densities above $1.5 \times 10^{18} \text{ cm}^{-2}$. These CHVCs were again claimed to be at extragalactic distance. However, surveys of local galaxy groups showed no detection of similar H I clouds (Zwaan 2001; Pisano et al. 2004). A more detailed study of a subsample of CHVCs concluded that they are most likely circumgalactic objects with distances of the order of 100 kpc (Westmeier, Brüns & Kerp 2005).

Many CHVCs have a head–tail morphology (Brüns et al. 2000; Putman, Saul & Mets 2011), suggesting that gas has been stripped via ram-pressure interaction with the ambient medium. A recent simulations of Salem et al. (2015) has shown such ram-pressure effect on the Large Magellanic Cloud (LMC). Some of the head–tail clouds have been studied in detail, such as HVC 125+41–207 (Brüns, Kerp & Pagels 2001), HVC 289+33+251 (Brüns & Westmeier 2004), HVC 291+26+195 and HVC 297+09+253 (Ben Bekhti et al. 2006, hereafter BBKW06). In many cases, they reveal two-component line profiles consisting of a cold core surrounded by a warm envelope. Nevertheless, numerical studies are somewhat inconclusive about the existence of two-phase structures in HVCs with z greater than ~ 20 kpc in a $T \sim 10^6 \text{ K}$ halo (Wolfire et al. 1995). Observationally, two-phase HVCs have been found in the MS and Leading Arm (LA) (e.g. see Stanimirović et al. 2008; For, Staveley-Smith & McClure-Griffiths 2013, hereafter FSM13;

*E-mail: biqing.for@uwa.edu.au (B-QF); lister.staveley-smith@uwa.edu.au (LS-S); naomi.mcclure-griffiths@anu.edu.au (NMMc-G)

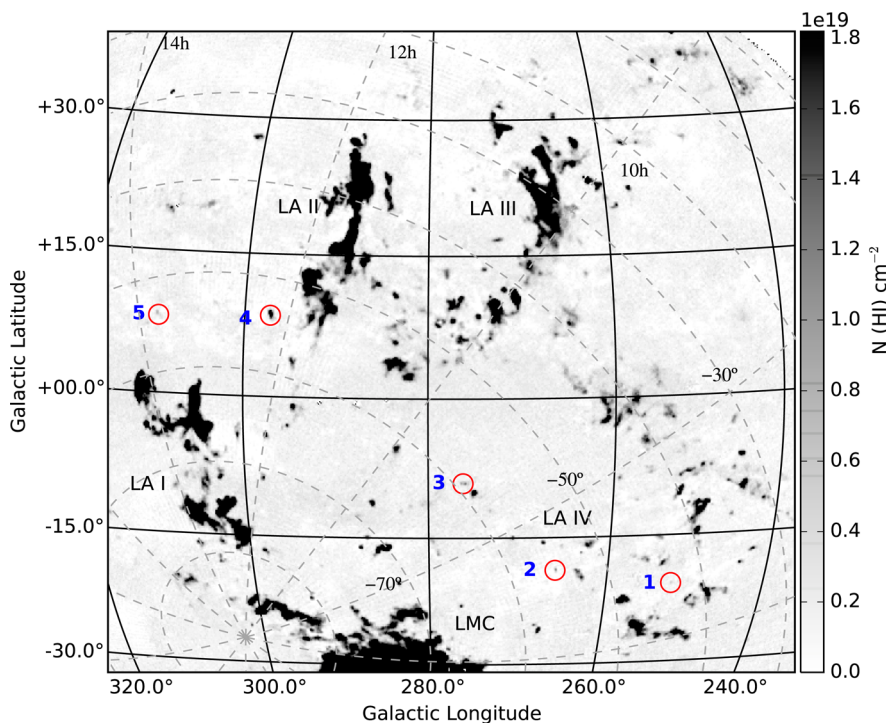


Figure 1. Integrated H I column density map in the region of the LA as studied by FSM13. The red circles mark the clouds selected for our ATCA observations at different Galactic latitudes. Equatorial coordinates are overlaid on the plot in dashed grey. The labels 1–5 correspond to HVC 252.2–20.5+310, HVC 266.0–18.7+338, HVC 276.3–09.0+277, HVC 297.1+08.5+253 and HVC 310.3+08.1+167, respectively. Three of the clouds are part of the LA IV.

For et al. 2014), which have estimated distances between 20 and 100 kpc. This implies that the thermal pressure and halo density beyond 10 kpc are not well understood.

In this paper, we study the multiphase structure of a subsample of HVCs in the region of the LA (FSM13). The aims are (1) to resolve any multiphase structure, (2) derive physical parameters, (3) study physical properties, in particular the thermal pressure in different regions to probe environmental effects. The paper is organized as follows: in Section 2, we list the selection criteria for the targets. Section 3 gives a description of our observational setup, data acquisition and reduction process. Section 4 describes the analysis methodology. Our results and interpretation are presented in Section 5. We compare the results with previous studies and discuss the implications for the Galactic halo by comparing our results with a model in Sections 6 and 7. Finally, a summary is given in Section 8.

2 TARGET SELECTION

We selected five HVCs from the FSM13 catalogue. The selection criteria are based on the following: (a) the peak brightness temperature of the HVC is $\sim 10\sigma$ above the brightness temperature sensitivity for the instrument setup and array configuration (see Section 3); (b) the HVC has a velocity linewidth of less than 10 km s^{-1} ; (c) the HVC has a distinct morphological type of head-tail, bow-shock or symmetric as described in FSM13; (d) the HVCs are over a range of different Galactic latitudes. Fig. 1 shows the integrated H I column density map of the LA region studied by FSM13, and the observed targets are marked with red circles.

3 OBSERVATIONS AND DATA

Both single-dish and interferometer data are used for this study. While single-dish data probe the diffuse emission, the interferom-

eter data allow us to probe small-scale structures. We employed data from the second data release of the single-dish Parkes Galactic All-Sky Survey (GASS; McClure-Griffiths et al. 2009) in this study. This has been corrected for stray radiation and radio frequency interference (Kalberla et al. 2010). GASS is an H I survey of the entire sky south of declination $+1^\circ$ using the 20-cm multibeam receiver on the Parkes radio telescope. GASS covers V_{LSR} between -400 and $+500 \text{ km s}^{-1}$. The data have a channel width of 0.82 km s^{-1} , a spectral resolution of 1 km s^{-1} , a brightness temperature (T_B) rms sensitivity of 57 mK , and an angular resolution of 16 arcmin . We refer the reader to detailed descriptions of GASS and data processing in McClure-Griffiths et al. (2009) and Kalberla et al. (2010).

The high-resolution H I observations were carried out at the Australia Telescope Compact Array (ATCA) in Narrabri using the EW367 and EW352 configurations in 2012 November and 2013 January, respectively. Only five out of the six antennas were used for the analysis. The inner five antennas of the EW367 configuration cover baselines between 92 and 367 m. The EW352 configuration covers baselines between 31 and 352 m. We used the zoom mode option of the Compact Array Broad-band Backend (CABB; Wilson et al. 2011) for the observations, which has a total bandwidth of 2 GHz with 1 MHz (coarse) and 0.5 kHz (fine) resolutions. We centred the zoom band on 1420 MHz . This configuration results in a velocity resolution of 0.1 km s^{-1} .

We observed the primary flux calibrator PKS 1934-638 at the beginning of each observing session. A secondary phase calibrator, which is located nearby the target field, was observed for 3 min every hour. Each observing session was about 10–12 h long, so achieved good uv -coverage. We also adopted the strategy of observing two targets per observing session by alternating between them. The beam was centred on the coordinates listed in the FSM13 catalogue.

The data reduction was performed in a standard manner using MIRIAD (Sault, Teuben & Wright 1995). To create dirty images,

we adopted robust weighting of 0 for four of the HVCs, which optimizes resolution and sensitivity. For HVC 310+08+167, a robustness parameter of 2 was used in order to match for its low surface brightness. A small selected region with H I emission in each dirty cube was deconvolved using the Steer CLEAN algorithm (Steer, Dewdney & Ito 1984). The final data cubes were corrected for primary beam attenuation and have an rms noise of about 10 mJy per beam.

To circumvent the short-spacing problem of the interferometer data, we combined the ATCA data with the single-dish data from GASS. We adopted the linear method, merging in the Fourier domain (Stanimirović 2002). With this method, the GASS data were converted to Jy per beam with a conversion factor of 0.658, re-gridded spatially and in velocity to match the ATCA image, and then the residual primary beam attenuation present in the ATCA data was applied to the GASS data prior to combining them. We smoothed the combined data cube spatially using the CONVOL task. The cubes are smoothed to full width half maxima (FWHM) of 150, 150, 160, 200 and 300 arcsec for HVC 252.2–20.5+310, HVC 266.0–18.7+338–18, HVC 276.3–09.0+277, HVC 297.1+08.5+253, HVC 310.3+08.1+167, respectively. We also smoothed the cubes spectrally over three channels using a Hanning function and extracted the channels that contain H I emission. As the sensitivity drops off quickly towards the outer edge of the beam, we used the ATCA primary beam model to mask out the noise at the outer edge of the data cube. Then, we created the integrated H I column density maps of five clouds as shown in Fig. 2.

4 ANALYSIS

We analyse the GASS and the combined ATCA and GASS data separately for each cloud. For the GASS data, spectra are extracted along the symmetry axis of each cloud to derive the physical parameters of peak H I column density (N_{HI}), velocity in the Local Standard of Rest frame (V_{LSR}) and velocity linewidth (Δv). In Figs 3–7, we show the extracted spectra (left), integrated H I column density map (top right) and the derived physical parameters along the symmetry axis (bottom right) for each cloud. The white crosses in the integrated H I column density map represent the positions of individual spectra along the sliced axis. The series of extracted spectra are fitted with either a single or double Gaussian profile, in which amplitude, velocity centre and variance are set as free parameters. Examples of double Gaussian fits are shown in Fig. 8. We calculate the integrated H I column density using $N_{\text{HI}} = 1.823 \times 10^{18} \int T_{\text{B}} dv = 1.823 \times 10^{18} \cdot T_{\text{B}} \cdot \sigma \sqrt{2\pi}$, where T_{B} is peak brightness temperature in K, v is the velocity in km s^{-1} , and σ is the standard deviation in km s^{-1} . The velocity linewidth is calculated using the derived σ , $\Delta v = \sigma \sqrt{8 \ln(2)}$. The derived results are shown in the bottom right panel of Figs 3–7, with red crosses indicating the narrow linewidth component of the cloud. The derived physical parameters using GASS data are summarized in Table 1.

For the combined data, we run a three-dimensional version of CLUMPFIND, which is an automatic routine for analysing clumpy structure in spectral line data cubes (Williams, de Geus & Blitz 1994). The routine searches the local peaks of the emission and follows them down to the user defined intensity level. We note that CLUMPFIND has its limitations if the data cube contains significant background noise. After running CLUMPFIND, we inspect the output manually to eliminate false detections. Identified clumps in each cloud are shown in Fig. 9 with crosses and labels. We perform a similar analysis as for the GASS data by extracting the spectra of

the clumps at peak H I column density and deriving their physical parameters. A summary of the derived physical parameters of these clumps is given in Table 2.

5 OVERALL PROPERTIES OF THE HVCs

Four of the HVCs studied here are classified as head–tail clouds. The only exception, HVC 266.0–18.7+338, is classified as a symmetric cloud by FSM13. However, the outer diffuse envelope makes the classification ambiguous. It may also be a head–tail cloud.

The head–tail morphology suggests ram–pressure interaction with the ambient medium. FSM13 reveal multiphase structures, which resemble broad and narrow components. We consider the broad component to be $> 10 \text{ km s}^{-1}$ in this study. On average, the velocity linewidths for the broad and narrow components are 20 km s^{-1} and 6.2 km s^{-1} , respectively. Most of the identified clumps only have a cold core. There are also unresolved clumps showing multiphase structures with broad and cold components or cold components only.

5.1 HVC 252.2–20.5+310

HVC 252.2–20.5+310 is part of the LA IV. The tail is pointing away from the Galactic plane. In Fig. 3, we show the spectral line profiles and derived physical parameters along the sliced axis of the cloud. The cloud is sliced from south to north with a designated position number. Multiphase structures of warm (broad) and cold (narrow) components at the head of the cloud are seen in the series of spectral line profiles. The rise and fall of the H I column density is gradual. There is no obvious velocity gradient across this cloud. We find that the cold component (red crosses) has a fairly consistent $V_{\text{LSR}} \sim 311 \text{ km s}^{-1}$. The FWHM of the warm component (black circles) varies in different parts of the cloud. The cold component has a typical linewidth of 7 km s^{-1} .

Fig. 2(a) shows the peak H I column density map of the combined image. The overlaid contour provides the spatial size of the cloud as observed by GASS. As seen in the figure, the head of the cloud has been resolved into two clumps. The morphology of these two clumps is outlined with contours in Fig. 9(a). Clumps A and B morphologically look like head–tail clouds which are pointing in the opposite direction. The derived physical parameters at the peak H I column density of both clumps are presented in Table 2. Clump A has two unresolved components, which have Δv of 2.80 and 7.38 km s^{-1} . Clump B is resolved with a single peak T_{B} of 2.78 K.

5.2 HVC 266.0–18.7+338

HVC 266.0–18.7+338 is also part of the LA IV. It is classified as a symmetric cloud in FSM13. The cloud is sliced from east to west, which corresponds to the spectral line profiles from top to bottom in Fig. 4. The cloud shows a clear velocity gradient with velocity decreasing from about 340 km s^{-1} to 332 km s^{-1} . In general, the cold component has a velocity larger than the warm component. The effect can be seen in the series of asymmetric spectral line profiles. The Δv of the warm component increases from the east end of the cloud and reaches a maximum at the centre before flattening it out to $\sim 25 \text{ km s}^{-1}$. A similar trend is seen in Δv of the cold component. The linewidth and velocity gradients indicate that this cloud is probably a head–tail cloud rather than a symmetric cloud.

The ATCA primary beam almost covers the entire cloud (see Fig. 2b). The combined image reveals a complex structure. Fig. 9

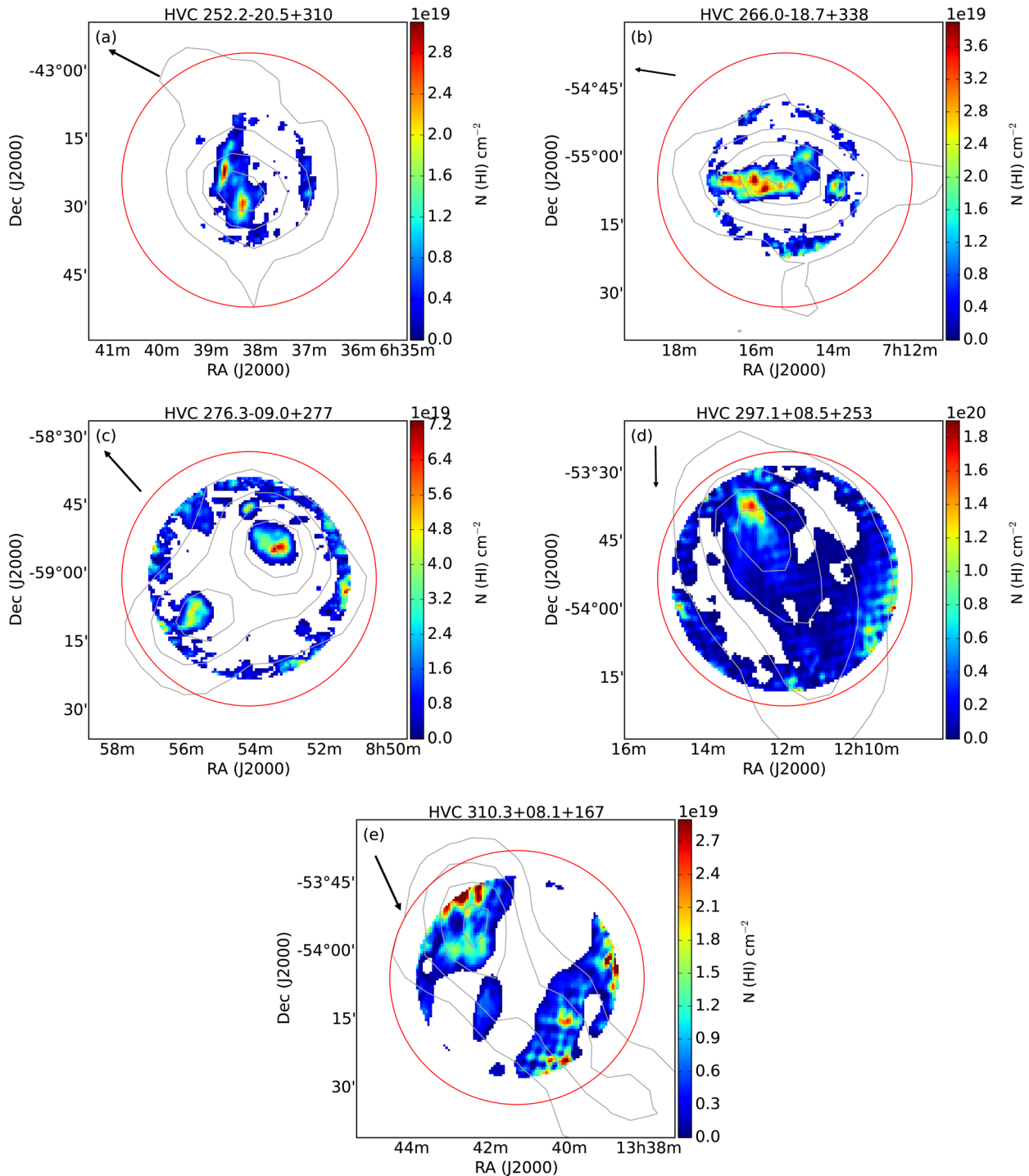


Figure 2. Integrated H I column density maps of the combined Parkes and ATCA H I data set. The red circles indicate the 12 per cent of peak sensitivity area of the image. The analysed regions as shown here are based on the percentage of the peak sensitivity. The grey contours represent H I column densities in the GASS data set. The arrows point in the direction of the Galactic plane.

shows a total of five distinct clumps identified via CLUMPFIND, named A–E. All clumps are resolved. These clumps have a fairly similar V_{LSR} (336–341 km s^{-1}). Clump D and E are considered warm with $\Delta v > 10 \text{ km s}^{-1}$. Both of them are also isolated from the main concentration of other clumps. None of them has a distinct morphology.

5.3 HVC 276.3–09.0+277

HVC 276.3–09.1+277 is the third HVC in this study that is located in LA IV. This head–tail cloud has two main cores with one being at the head of the cloud and the other at the tail (see Fig. 5). The analysis is performed by slicing the cloud diagonally from south-east to north-west. The cloud does not show a clear velocity gradient.

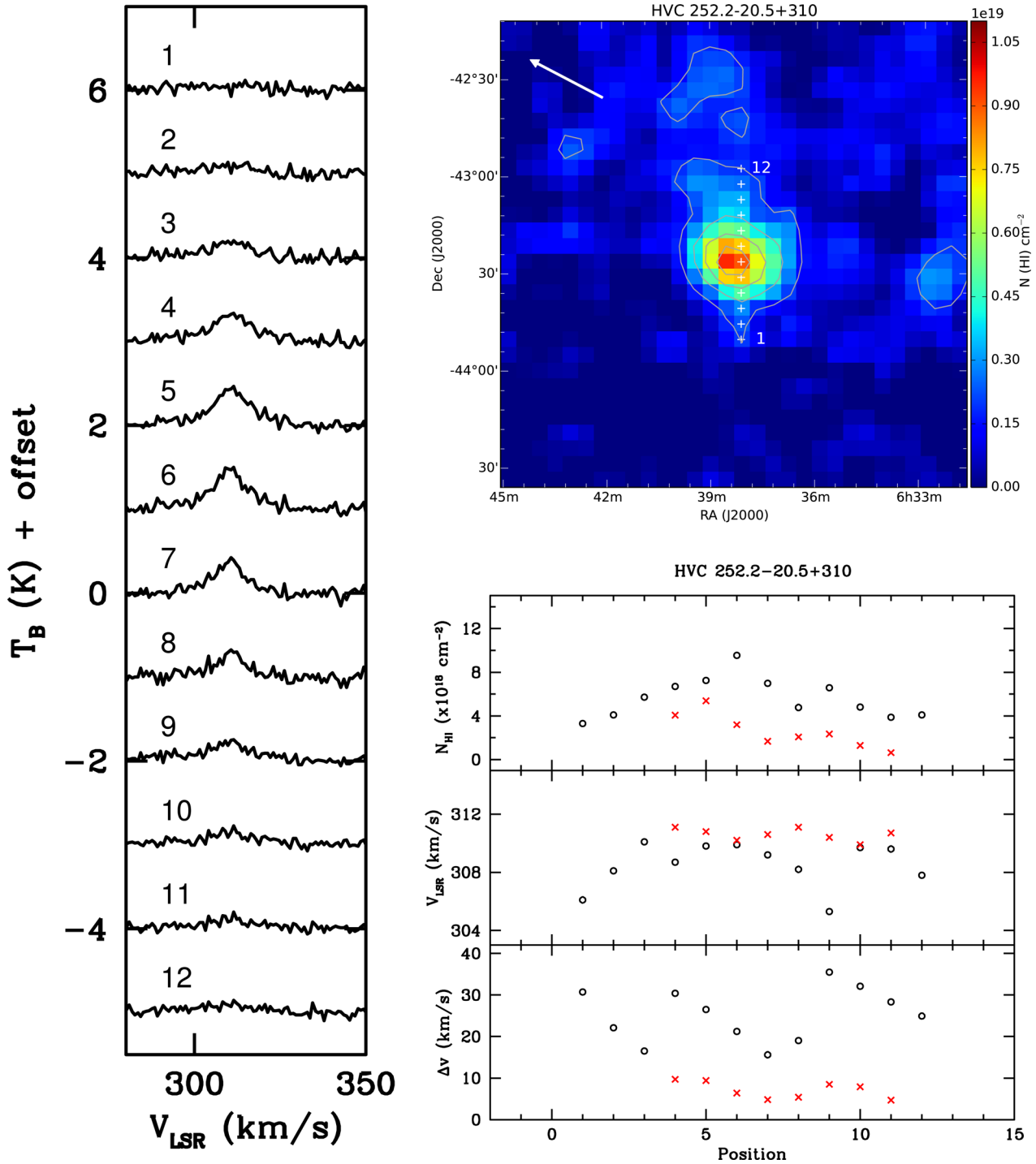


Figure 3. Top right: integrated H I column density map of HVC 252.2–20.5+310 in the GASS data set. The contour levels correspond to H I column densities (N_{HI}) of 0.2, 0.4, 0.6, 0.8, $1.0 \times 10^{19} \text{ cm}^{-2}$. The white crosses represent the positions along the sliced axis of the cloud. It is sliced from south to north with a designated position number. The arrow points in the direction of the Galactic plane. Left: series of extracted spectra along the sliced axis. Bottom right: physical parameters of the cloud as derived from the spectra. Black circles and red crosses represent the broad and narrow components, respectively.

Its head is rather compressed. The average Δv for all of the cold components is 7.5 km s^{-1} . The V_{LSR} values of the cold components decrease gradually and are larger than the warm components. The peak T_{B} is $\sim 0.7 \text{ K}$ at the main core of the cloud.

In Figs 2(c) and 9(c), we show the resolved clumps in the combined image. Three clumps are identified. Clump A is located in

the main core of the cloud but clump B is displaced slightly from the second core of the cloud as seen in the diffuse emission. Both clump A and B are morphologically similar to head–tail clouds. Clump C is relatively smaller than clump A and B. It is unresolved and consists of two cold components, which have Δv of 3.25 and 9.44 km s^{-1} .

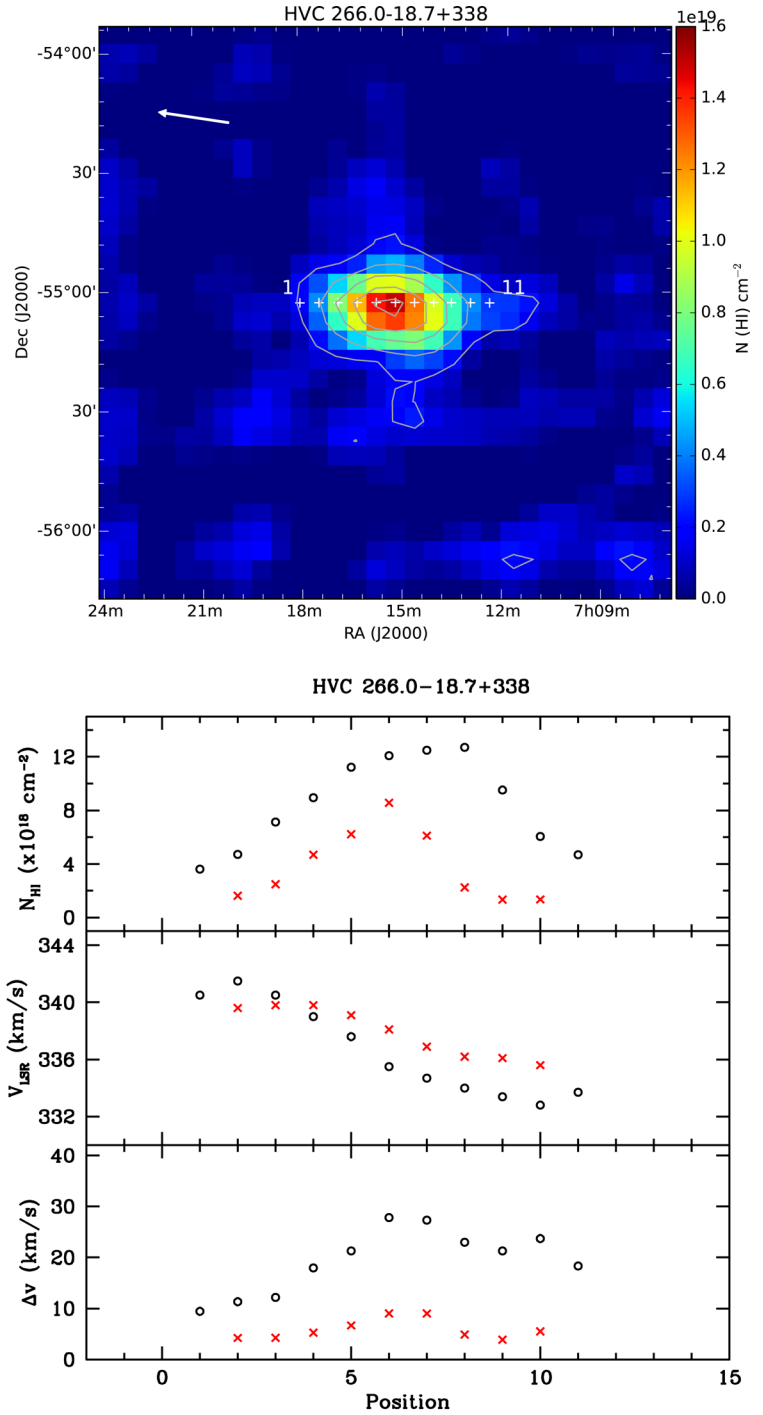
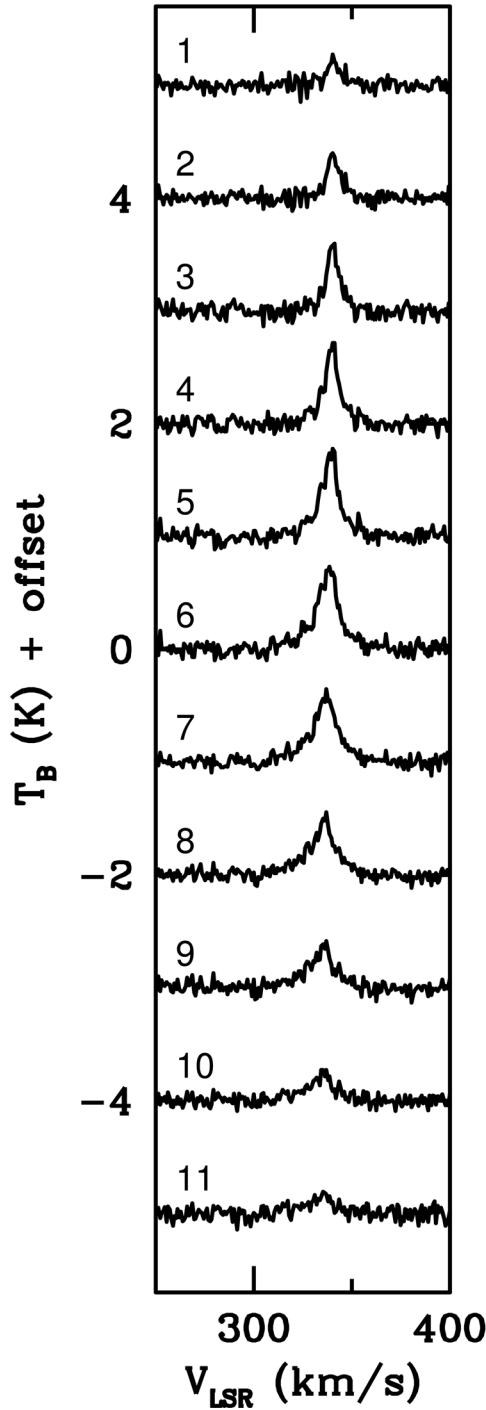


Figure 4. Same as Fig. 3 except for HVC 266.0–18.7+338. The contour levels correspond to 0.2, 0.5, 0.8, 1.1, $1.40 \times 10^{19} \text{ cm}^{-2}$ and the cloud is sliced from east to west.

5.4 HVC 297.1+08.5+253

HVC 297.1+08.5+253 is situated in the vicinity between LA I and II, closer to the south-eastern part of LA II. This head–tail cloud is morphologically slightly different from HVC 252.2–20.5+210. The contours show a typical head–tail structure (see Fig. 6). The tail of HVC 297.1+08.5+253 is pointing away from the Galactic plane.

In Fig. 6, the spectral line profiles (top to bottom) represent the sliced positions of the cloud from south-west to north-east. As

expected, the peak H I column density increases towards the head of the cloud. Interestingly, the derived H I column density of the warm component reaches its maximum (position 8) before the maximum H I column densities as shown in the GASS integrated H I column density map at positions 9 and 10. The cold component also shows the same rise and fall pattern in H I column density but with the maximum at position 11. The V_{LSR} shows a small gradient in the tail of the cloud and then becomes constant at 253 km s^{-1} for both cold and warm components. Half of the cloud consists of warm

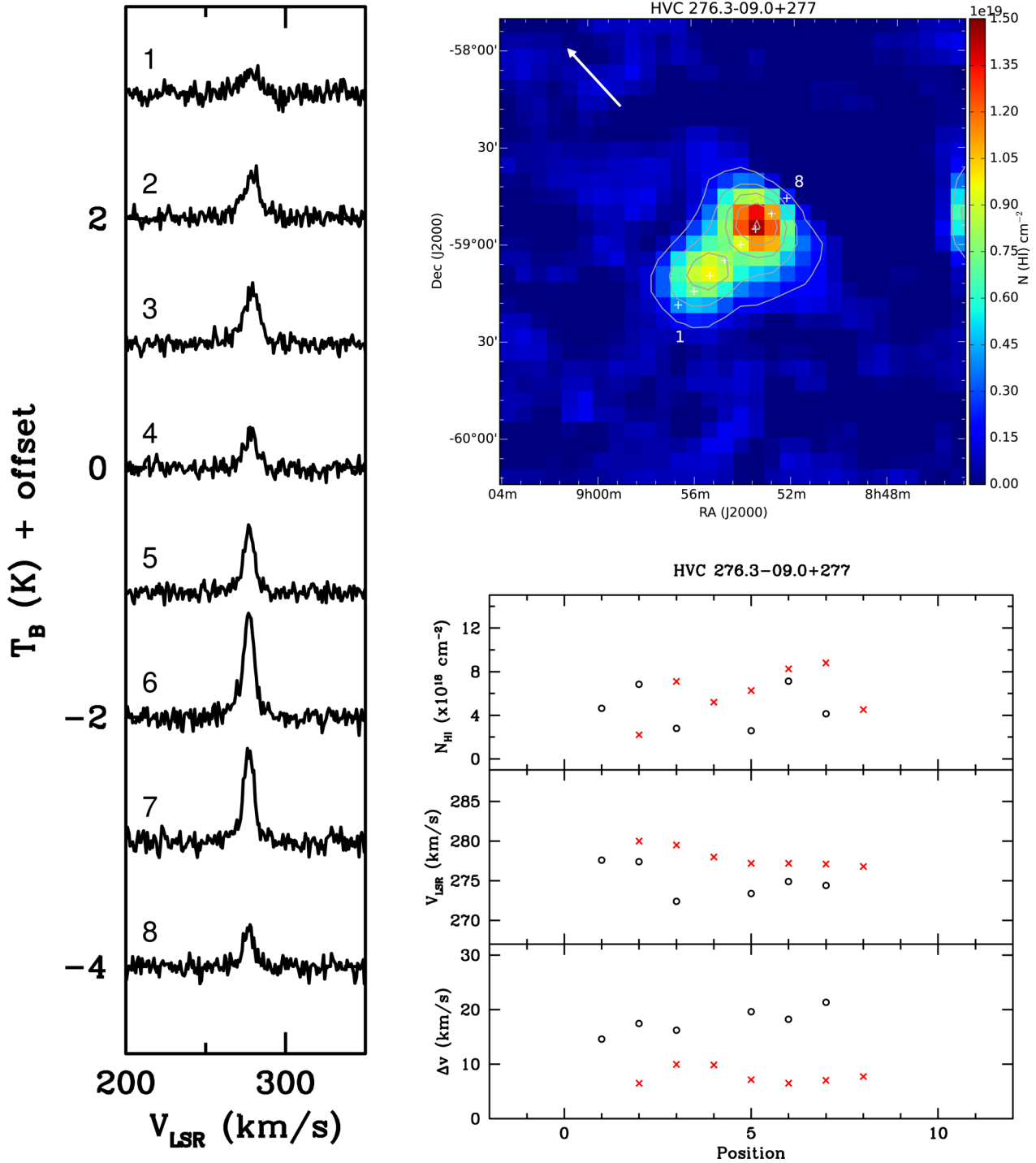


Figure 5. Same as Fig. 3 except for HVC 276.3–09.0+277. The contour levels correspond to $0.2, 0.5, 0.8, 1.1, 1.40 \times 10^{19} \text{ cm}^{-2}$ and the cloud is sliced from south-east to north-west.

component only, with an average velocity linewidth of 20.1 km s^{-1} . At position 14, two components are detected (refer bottom panel of Fig. 6). These two components on average have a velocity linewidth of 4.1 km s^{-1} .

The cloud is relatively diffuse as shown in the combined image (Fig. 2d). The main resolved feature is offset and leading the diffuse core of the cloud as seen in the GASS image. This explains why the H I column density of the cold component peaks at position 11 in

the analysis of the GASS image. Fig. 9(d) shows the resolved feature and two detected clumps. Unfortunately, the feature is detected fairly close to the edge of the ATCA beam, where sensitivity drops off significantly. Thus, extended features cannot be seen.

Clump A has the highest T_B ($\sim 20.3 \text{ K}$) amongst the detected clumps in this study. Clump A is resolved and reveals sub-components as seen in its spectral line profile (not shown here). The resolved clump B has Δv of $\sim 5 \text{ km s}^{-1}$.

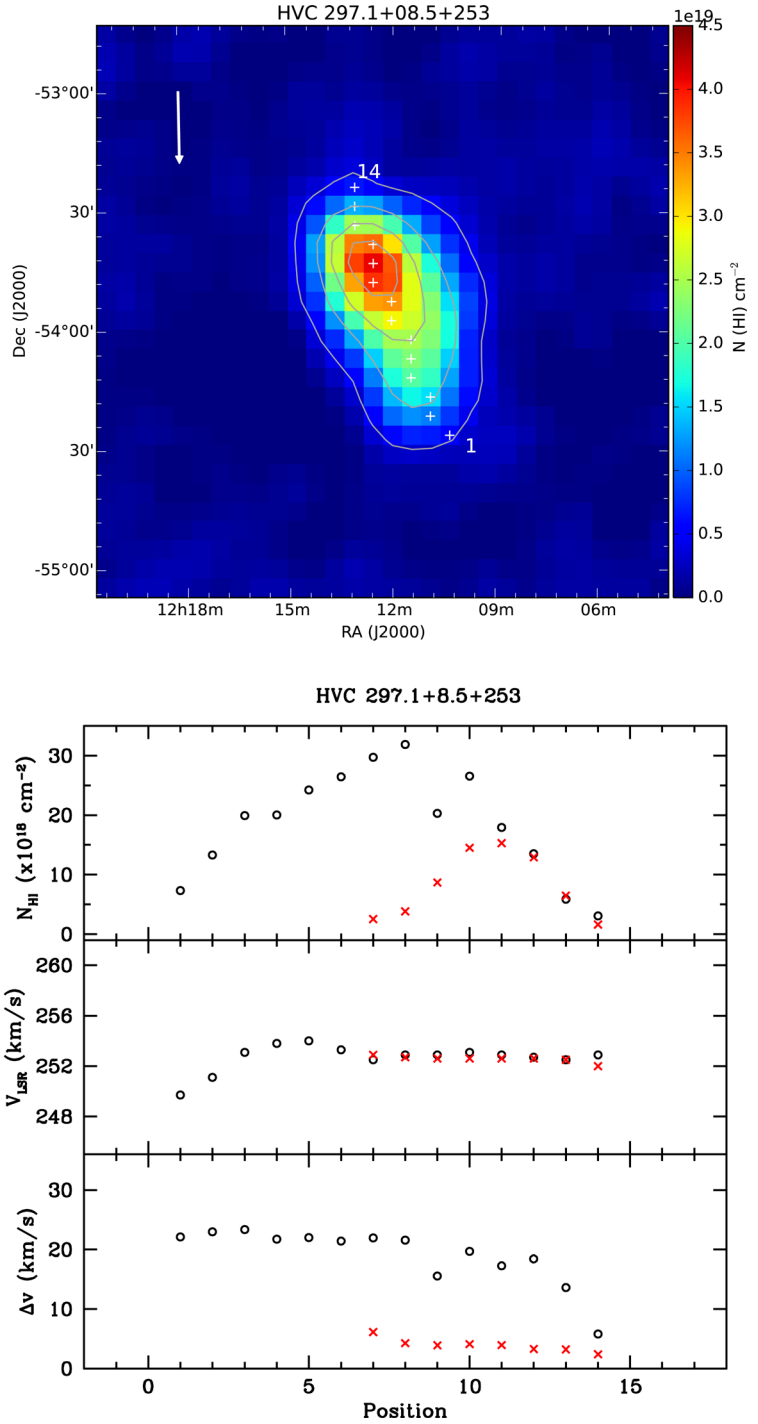
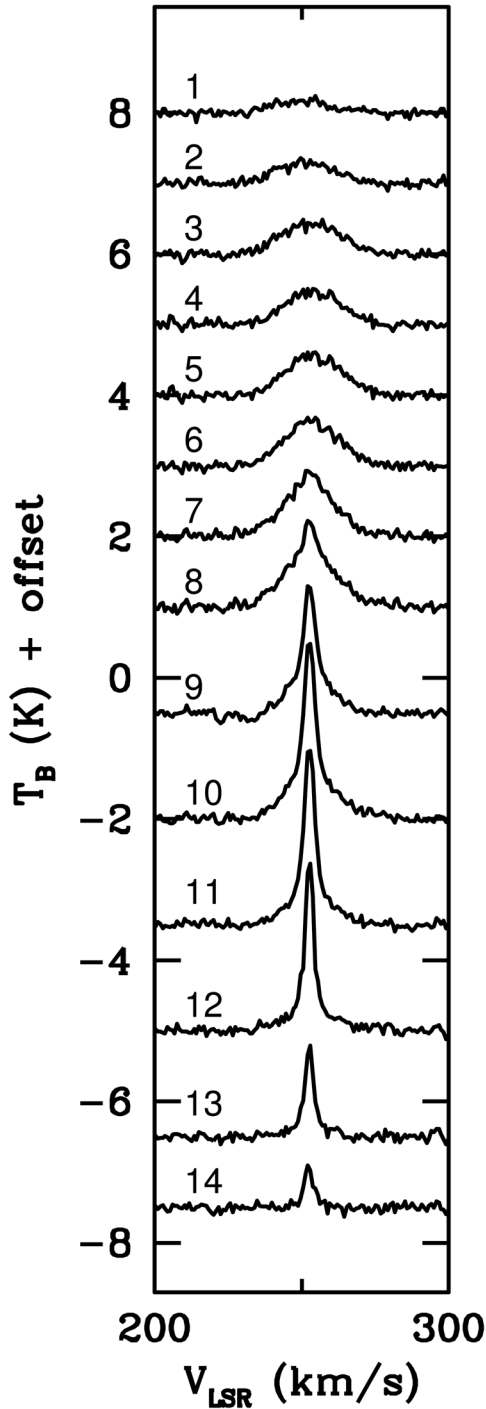


Figure 6. Same as Fig. 3 except for HVC 297.1+08.5+253. The contour levels correspond to $0.5, 1.5, 2.5, 3.5, 4.5 \times 10^{19} \text{ cm}^{-2}$ and the cloud is sliced from south-west to north-east.

5.5 HVC 310.3+08.1+167

HVC 310.3+08.1+167 is located north of LA I. It is pointing in the general direction of motion of LA I. This cloud is quite diffuse compared to the other clouds in this study, It has a very long diffuse tail, which spans nearly $1^\circ.5$, and a slight kink at the end (see Fig. 7). While this cloud has a lower V_{LSR} than other selected HVCs in this study, it is assumed to be part of the LA based on the constraints listed in FSM13 to exclude the Galactic H I emission.

The analysis is performed by slicing along the symmetry axis from south-west to north-east. The spectral line profiles show that the cloud has a fairly low brightness temperature of ~ 0.4 K. The multiple peaks of H I column density indicate numerous components. Apart from the two deviating points at positions 12 and 13 in the velocity plot, the gradual increase of V_{LSR} suggests that the cloud has a velocity gradient.

The contours in Fig. 2(e) show that the size of the cloud is a lot larger than the ATCA beam. Since its coordinates were derived at

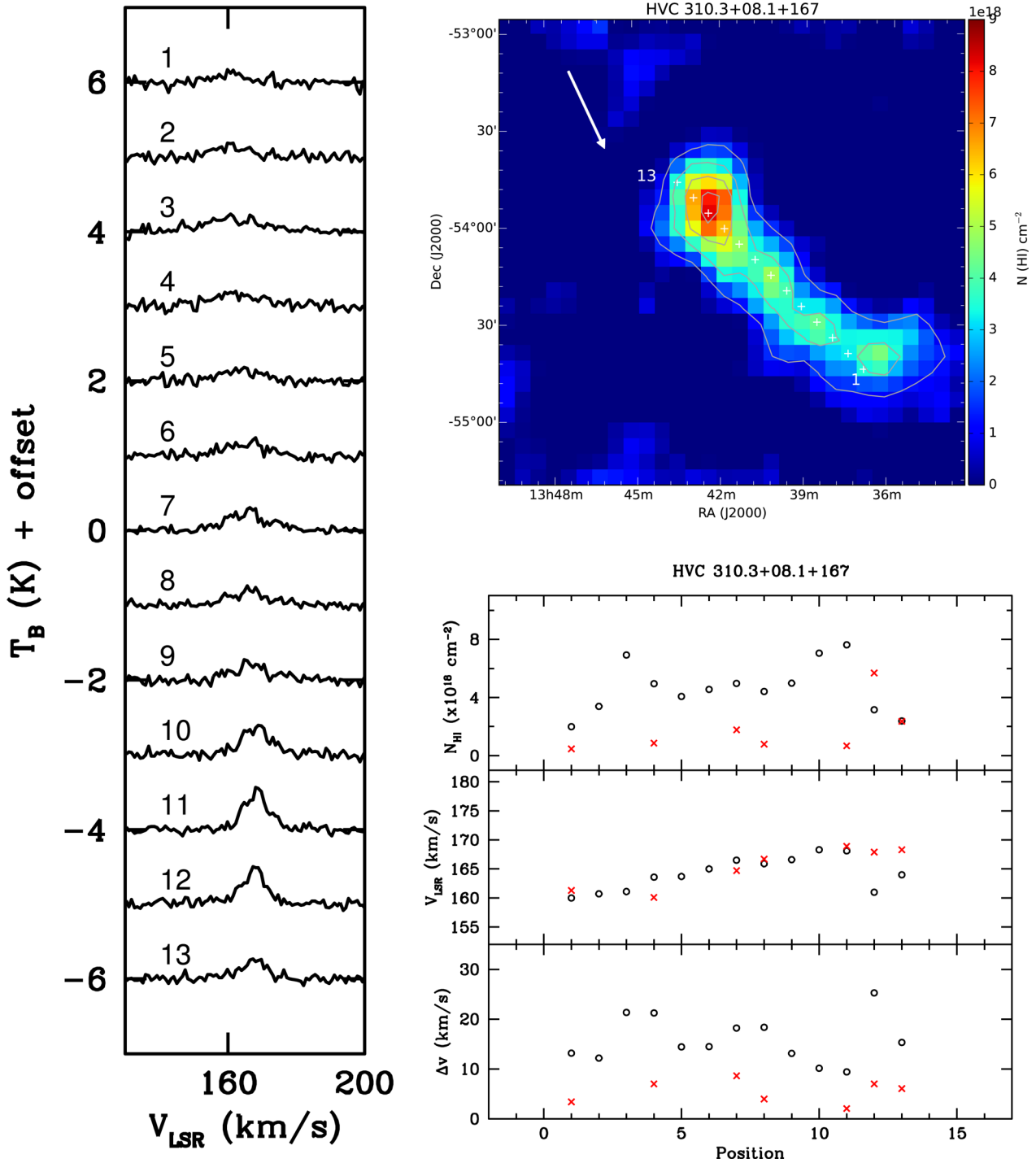


Figure 7. Same as Fig. 3 except for HVC 310.3+08.1+167. The contour levels correspond to $1.5, 3.5, 5.5, 7.5, 9.5 \times 10^{18} \text{ cm}^{-2}$ and the cloud is sliced from south-west to north-east.

the axis centre of the cloud, the core structure was not observed at the centre of the ATCA beam, where sensitivity is highest. The low surface brightness nature of the cloud also makes clump identification harder. The identification and derivation of physical parameters of the clumps were performed on the smoothed cube. Six distinct clumps have been identified (see Fig. 9e). All of them are unresolved and have sub-components. The sub-components are cold as well.

The structure near the head is complex with five clumps being detected within the sensitivity cutoff. They have V_{LSR} ranging from

165 to 172 km s^{-1} . Clump F has a lower V_{LSR} of 161.6 km s^{-1} . They all appear to have an irregular shape.

6 COMPARISON WITH PREVIOUS STUDIES

Two additional compact HVCs, HVC 291+26+195 and HVC 297+09+253, were observed and studied in high resolution by [BBKW06](#). Both clouds are associated with the LA. [BBKW06](#) analysed the data obtained from the Parkes HI survey of the

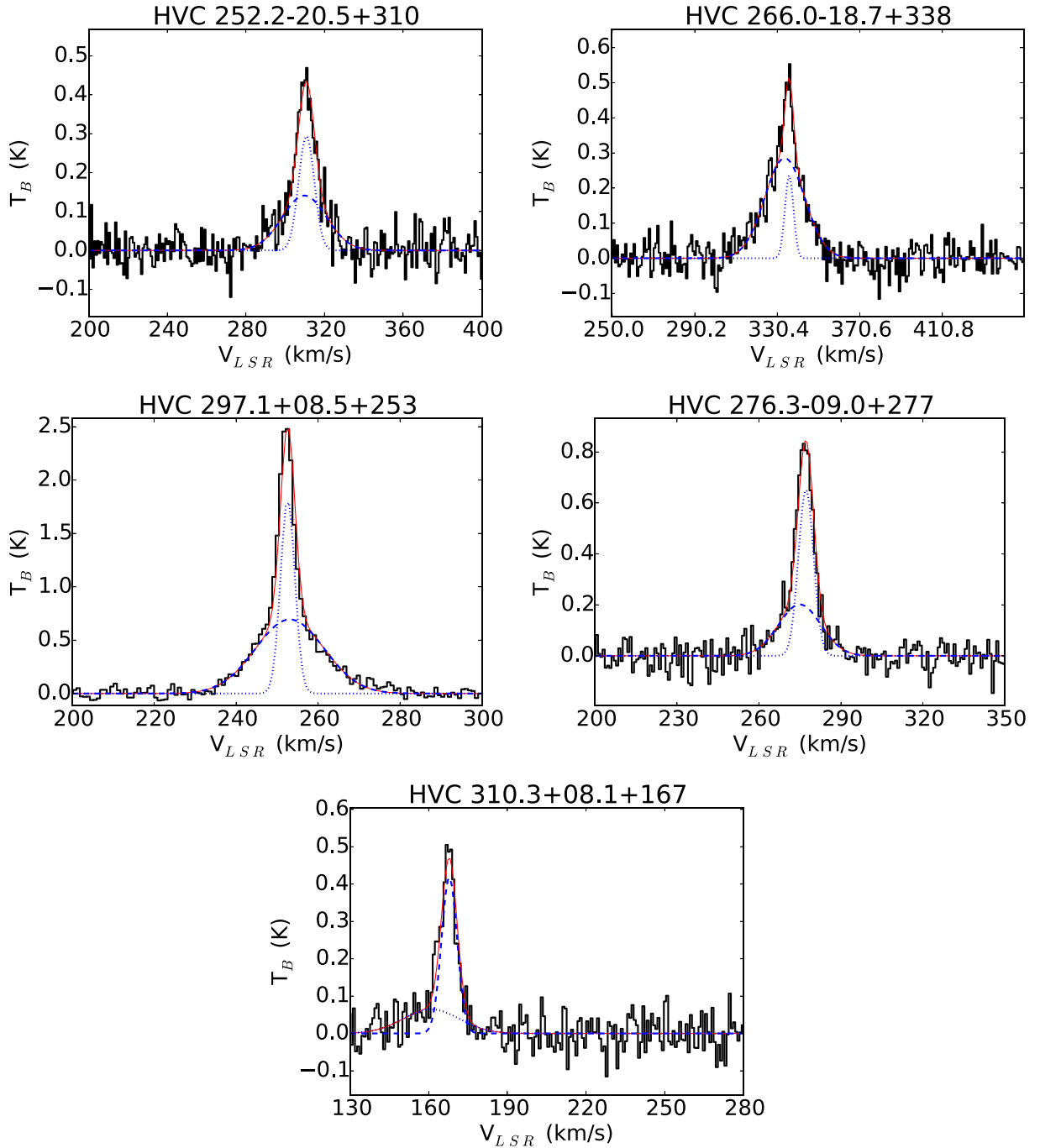


Figure 8. Examples of double Gaussian fits to a spectrum from each cloud. Solid line (red) indicates the combined profile of the two Gaussian profiles.

Magellanic System (Brüns et al. 2005) and interferometer data observed with the 750D configuration of the ATCA. By comparing with our integrated H I column density map of the ATCA data alone (not shown here), we find similar resolved structures as seen in fig. 4 of BBKW06. They identified 17 clumps, which is more than detected in our study, although the method of identification is different. They did not analyse the combined Parkes and ATCA data.

Another high-resolution study of a compact HVC (HVC 289+33+251) has been carried out by Brüns & Westmeier (2004). This cloud is also in the vicinity of LA but a distance of 150 kpc was assumed, which is further than the typical distance of the Magellanic Clouds (50 kpc). This cloud is significantly brighter

than our observed targets and has the typical head–tail morphology. It is relatively compact as well. A direct quantitative comparison cannot be achieved due to different resolutions of the two studies.

7 DISCUSSION

7.1 HVC phase diagram

HVCs may exist as a stable two-phase medium if the halo pressure lies within a certain range, $P_{\min} < P < P_{\max}$, where P_{\min} and P_{\max} are a function of height, z , above the Galactic plane (Wolfire et al.

Table 1. Derived physical parameters of each cloud using either a single or double Gaussian profile. GASS data are used and the position number represents the location of extracted spectrum.

Name	Position no.	T_{B1} (K)	T_{B2} (K)	V_{LSR1} (km s ⁻¹)	V_{LSR2} (km s ⁻¹)	N_{HI1} (10 ¹⁸ cm ⁻²)	N_{HI2} (10 ¹⁸ cm ⁻²)	Δv_1 (km s ⁻¹)	Δv_2 (km s ⁻¹)
HVC 252.2–20.5+310	1	...	0.06	...	306.1	...	3.30	...	30.7
	2	...	0.10	...	308.1	...	4.09	...	22.1
	3	...	0.18	...	310.1	...	5.71	...	16.5
	4	0.22	0.11	311.1	308.7	4.07	6.70	9.7	30.4
	5	0.29	0.14	310.8	309.8	5.38	7.24	9.4	26.5
	6	0.26	0.23	310.2	309.9	3.19	9.55	6.4	21.2
	7	0.18	0.23	310.6	309.2	1.67	6.98	4.8	15.6
	8	0.20	0.13	311.1	308.2	2.07	4.77	5.4	19.0
	9	0.14	0.10	310.4	305.3	2.34	6.57	8.5	35.5
	10	0.08	0.08	309.9	309.7	1.29	4.81	7.9	32.1
	11	0.07	0.07	310.7	309.6	0.63	3.87	4.7	28.3
	12	...	0.08	...	307.8	...	4.08	...	24.9
HVC 266.0–18.7+338	1	0.20	...	340.5	...	3.61	...	9.4	...
	2	0.20	0.21	339.6	341.5	1.63	4.71	4.2	11.3
	3	0.30	0.30	339.8	340.5	2.48	7.13	4.3	12.2
	4	0.46	0.26	339.8	339.0	4.68	8.94	5.3	18.0
	5	0.48	0.27	339.1	337.6	6.22	11.21	6.7	21.3
	6	0.49	0.22	338.1	335.5	8.56	12.09	9.1	27.8
	7	0.35	0.24	336.9	334.7	6.11	12.49	9.0	27.3
	8	0.24	0.29	336.2	334.0	2.24	12.71	4.9	23.0
	9	0.18	0.23	336.1	333.4	1.34	9.51	3.9	21.3
	10	0.13	0.13	335.6	332.8	1.35	6.06	5.5	23.7
	11	...	0.13	...	333.7	...	4.68	...	18.3
HVC 276.03–09.0+277	1	...	0.16	...	277.6	...	4.64	...	14.6
	2	0.18	0.20	280.0	277.4	2.21	6.84	6.5	17.4
	3	0.37	0.09	279.5	272.4	7.10	2.80	10.0	16.2
	4	0.27	...	278.0	...	5.20	...	9.9	...
	5	0.45	0.07	277.2	273.4	6.27	2.59	7.1	19.6
	6	0.65	0.20	277.2	274.9	8.26	7.12	6.5	18.2
	7	0.65	0.10	277.1	274.4	8.80	4.13	7.0	21.3
	8	0.30	...	276.8	...	4.52	...	7.7	...
HVC 297.1+08.5+253	1	...	0.17	...	249.7	...	7.31	...	22.1
	2	...	0.30	...	251.1	...	13.30	...	23.0
	3	...	0.44	...	253.1	...	19.92	...	23.4
	4	...	0.47	...	253.8	...	20.05	...	21.8
	5	...	0.57	...	254.0	...	24.23	...	22.0
	6	...	0.64	...	253.3	...	26.46	...	21.4
	7	0.21	0.70	252.9	252.5	2.55	29.74	6.1	22.0
	8	0.46	0.76	252.7	252.9	3.81	31.90	4.3	21.6
	9	1.15	0.67	252.6	252.9	8.69	20.31	3.9	15.5
	10	1.82	0.69	252.6	253.1	14.52	26.57	4.1	19.7
	11	1.99	0.54	252.6	252.9	15.28	17.92	4.0	17.3
	12	2.02	0.38	252.6	252.7	12.92	13.54	3.3	18.4
	13	1.03	0.22	252.5	252.5	6.45	5.87	3.2	13.6
	14	0.35	0.27	252.0	252.9	1.62	3.05	2.4	5.8
HVC 310.3+08.1+167	1	0.07	0.08	161.3	160.0	0.46	1.99	3.4	13.2
	2	...	0.14	...	160.7	...	3.39	...	12.2
	3	...	0.17	...	161.1	...	6.93	...	21.3
	4	0.06	0.12	160.1	163.6	0.86	4.95	7.0	21.3
	5	...	0.15	...	163.7	...	4.07	...	14.4
	6	...	0.16	...	165.0	...	4.56	...	14.5
	7	0.11	0.14	164.7	166.5	1.77	4.97	8.6	18.2
	8	0.10	0.12	166.7	165.9	0.79	4.41	4.0	18.4
	9	...	0.20	...	166.6	...	4.98	...	13.1
	10	...	0.36	...	168.3	...	7.05	...	10.1
	11	0.17	0.42	168.9	168.1	0.67	7.63	2.1	9.4
	12	0.42	0.06	167.9	161.0	5.69	3.16	7.0	25.3
	13	0.20	0.08	168.3	164.0	2.36	2.38	6.1	15.3

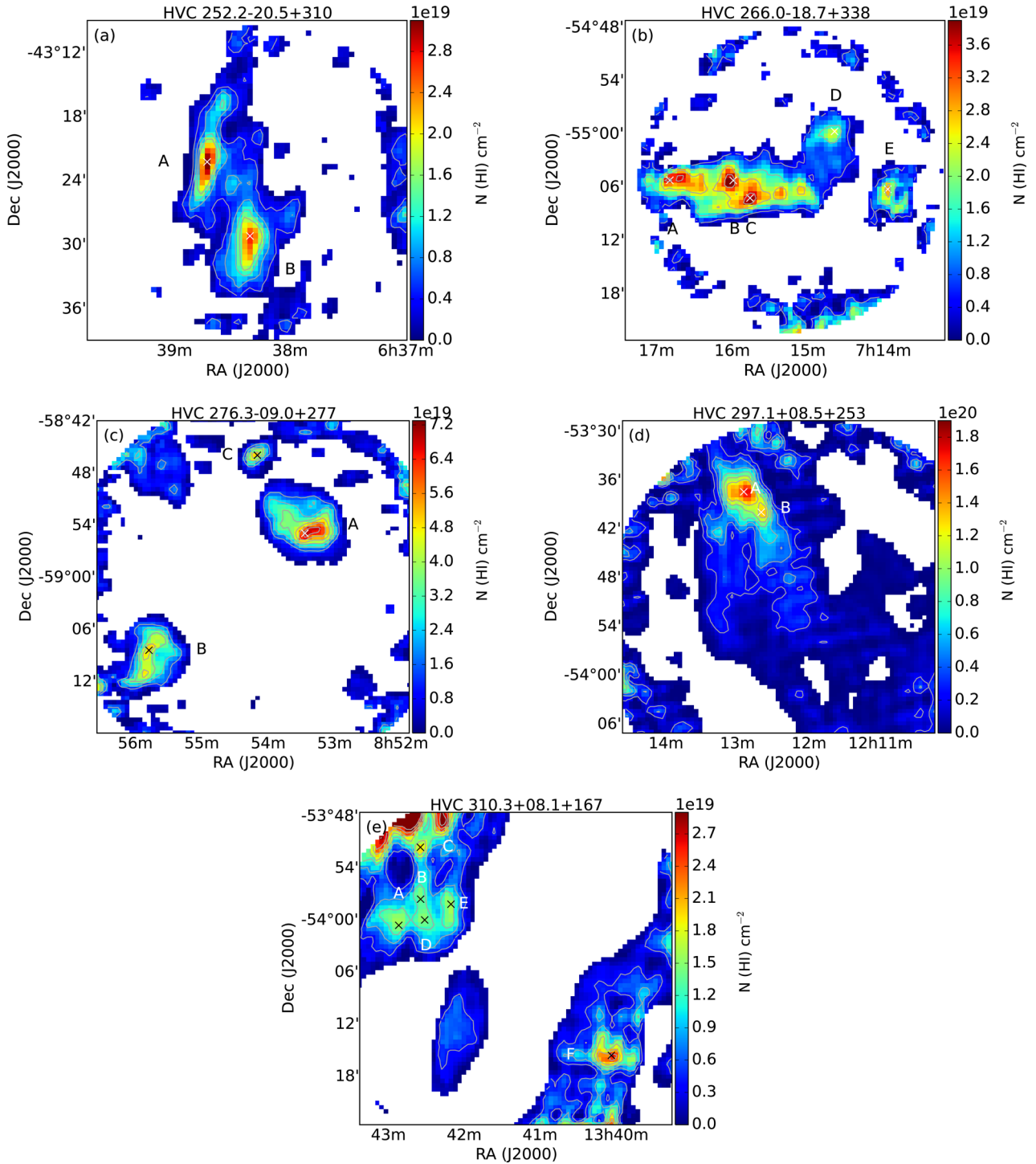


Figure 9. Integrated H I column density maps of the combined Parkes and ATCA H I data sets. Identified clumps are marked with a cross and are labelled. Contours are plotted to highlight the morphology of the clumps.

1995). The phase diagram of thermal pressure, P , versus hydrogen density, n , can be used to examine the stability of HVCs. To calculate the thermal pressure of the resolved clumps, we apply the ideal gas law, $P/k = nT_k$, where k is the Boltzmann constant, n is the hydrogen density and T_k is the kinetic gas temperature. The upper limit of the kinetic gas temperature can be derived from the velocity linewidth assuming the observed linewidth is dominated by Doppler broadening, $T_k = m_H \Delta v^2 / (8 k \ln 2) = 21.8 (\Delta v / \text{km s}^{-1})^2$, where

$m_H = 1.674 \times 10^{-27}$ kg. Assuming spherical symmetry for the clump, $n = N_{H I} / (d \tan \theta)$, where θ is the angular diameter of the clump and d is the distance to the cloud. The hydrogen density is calculated by assuming distances to the cloud of 25 and 50 kpc. The former distance is close to the kinematic distance derived in McClure-Griffiths et al. (2008). The latter is close to the measured distance of the LMC (Pietrzyński et al. 2013). Calculated values are presented in Table 2.

Table 2. Derived physical parameters and location of each clump found in the combined data.

Name	Clump	RA	Dec.	T_{B1} (K)	T_{B2} (K)	V_{LSR1} (km s ⁻¹)	V_{LSR2} (km s ⁻¹)	N_{HI} (10 ¹⁹ cm ⁻²)	N_{HI2} (10 ¹⁹ cm ⁻²)	Δv_1 (km s ⁻¹)	Δv_2 (km s ⁻¹)	T_k (K)	θ (°)	n^b (cm ⁻³)	P/k^b (k cm ⁻³)
HVC 252.2–20.5+310	A	06 ^h 38 ^m 42.26	–43°22′14″43	3.49	1.27	312.5	313.4	1.89	1.82	2.80	7.38
HVC 266.0–18.7+338	B	06 ^h 38 ^m 20.27	–43°29′14″73	2.78	...	310.8	...	2.50	...	4.65	...	471.37	0.144	0.13	60.78
	A	07 ^h 16 ^m 36.77	–55°05′14″92	3.29	...	340.9	...	4.04	...	6.33	...	872.96	0.052	0.58	503.19
HVC 276.03–09.0+277	B	07 ^h 16 ^m 01.82	–55°05′16″69	3.78	...	341.3	...	4.34	...	5.92	...	764.99	0.040	0.80	610.84
	C	07 ^h 15 ^m 44.38	–55°07′17″20	3.52	...	339.5	...	4.37	...	6.40	...	893.88	0.048	0.68	604.95
HVC 297.1+08.5+253	D	07 ^h 14 ^m 38.03	–54°59′46″95	1.24	...	338.2	...	2.51	...	10.41	...	2361.77	0.056	0.33	779.77
	E	07 ^h 13 ^m 55.98	–55°06′15″34	2.07	...	336.0	...	5.28	...	13.16	...	3772.62	0.049	0.80	3017.05
HVC 310.3+08.1+167 ^a	A	08 ^h 53 ^m 26.09	–58°54′57″38	6.67	...	276.5	...	7.95	...	6.14	...	823.07	0.056	1.05	864.63
	B	08 ^h 55 ^m 46.20	–59°08′54″81	3.69	...	281.0	...	4.70	...	6.56	...	937.18	0.042	0.83	781.87
HVC 297.1+08.5+253	C	08 ^h 54 ^m 08.70	–58°45′56″93	2.39	5.99	273.5	275.5	4.39	3.78	9.44	3.25
	A	12 ^h 12 ^m 51.88	–53°37′28″63	20.29	4.38	252.8	249.5	12.99	1.88	3.30	2.21
HVC 310.3+08.1+167 ^a	B	12 ^h 12 ^m 38.40	–53°39′29″49	11.69	...	252.9	...	11.13	...	4.91	...	524.91	0.028	3.00	1572.20
	A	13 ^h 42 ^m 50.09	–54°00′33″46	0.72	0.23	165.5	172.3	0.70	0.15	5.02
HVC 297.1+08.5+253	B	13 ^h 42 ^m 32.98	–53°57′34″32	0.30	0.61	172.2	166.2	0.21	0.70	3.56	5.94
	C	13 ^h 42 ^m 32.80	–53°51′33″45	0.29	0.57	163.5	169.5	0.26	0.59	4.69	5.34
HVC 297.1+08.5+253	D	13 ^h 42 ^m 29.65	–54°00′04″75	0.29	0.55	172.5	166.6	0.20	0.63	3.42	5.86
	E	13 ^h 42 ^m 09.20	–53°58′05″56	0.32	0.12	171.9	167.1	0.28	0.11	4.56	4.63
HVC 297.1+08.5+253	F	13 ^h 40 ^m 02.87	–54°15′34″20	0.28	0.16	167.4	161.6	0.31	0.17	5.57	5.47

Notes. ^aParameters are derived from a spatially and spectrally smoothed data cube.

^bAssuming a distance of 25 kpc.

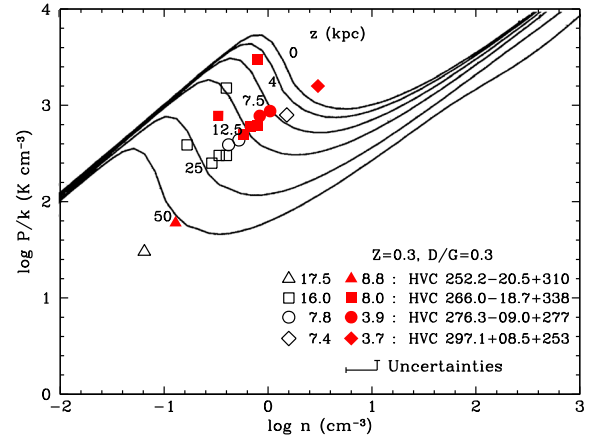


Figure 10. Thermal pressure, P/k , versus hydrogen density, n , for various heights, z , above the Galactic plane in kpc. The model of $Z = D/G = 0.3$ is taken from Wolfire et al. (1995). Filled and non-filled symbols represent the calculated data points by assuming a distance of 25 and 50 kpc, respectively. The value next to the symbols in the legend is the calculated heights z , in kpc.

Fig. 10 shows the phase diagram at different heights z above the Galactic plane overplotted with our derived P/k and n for the resolved clumps. Filled and non-filled symbols correspond to the calculated data points by assuming a distance of 25 and 50 kpc, respectively. The inferred z with the assumed distance for each HVC clump is listed next to each symbol. We note that the phase diagram is sensitive to the metallicity (Z) and dust-to-gas ratio (D/G). We adopt the model of $Z = D/G = 0.3$, which is appropriate for stripped LMC gas (Wolfire et al. 1995).

To estimate the effects of uncertainties in our derived P/k and n , we consider various scenarios. Assuming the observed clump is not of spherical shape but an ellipsoid, viewing along the major axis gives a larger angular diameter. Twice the size in angular diameter will result in a decrease in hydrogen gas density by a factor of 2. The derived T_k is an upper limit given by the velocity linewidth. A decrease of T_k by 100 K will result in +0.1 change in $\log P/k$. Ignoring the two data points near the 50 kpc curve and taking into account the uncertainties, we find that majority of the data points fall on to their corresponding z for the phase diagram. Also, the data points lie in the instability valley of the two-phase medium.

7.2 Halo environment as a function of galactic latitude

If we assume that the clumps are in hydrostatic equilibrium, the thermal pressure of the clump is equal to the external halo thermal pressure. In Fig. 11, we show the average physical parameters of the resolved clumps for each cloud as a function of Galactic latitude. In this case, Galactic latitude is a proxy for z . The height z decreases from negative to positive Galactic latitude. Interestingly, we find a trend of increasing halo thermal pressure, hydrogen density and H I column density with increasing Galactic latitude. This suggests that the clouds reside in a denser halo environment at more positive Galactic latitude. While it has been suggested that the LA is closer to the Galactic Centre than the LMC (McClure-Griffiths et al. 2008), this is the first evidence showing a possible distance gradient in the LA region using compact HVCs that span over $\sim 80^\circ$ in Galactic longitude. The leading part of the LA (LA II and LA III) is most likely closer to our Galaxy than the LA I, which has a kinematic distance of ~ 21 kpc (McClure-Griffiths et al. 2008). The study of

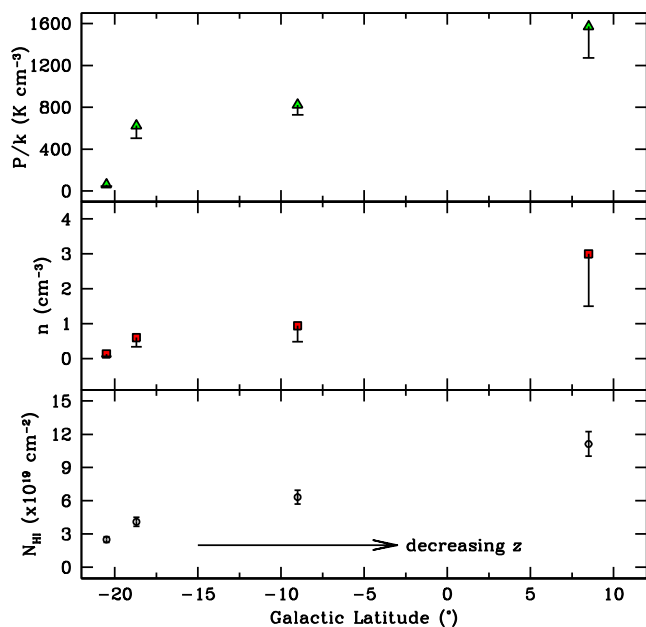


Figure 11. Thermal pressure, P/k , hydrogen density, n , and H I column density, $N_{\text{H I}}$, as a function of Galactic latitude (as a proxy of z). Each data point represents the average physical parameters of all resolved clumps for each cloud. A distance of 25 kpc is assumed here. Uncertainties of P/k and n are discussed in Section 7.1. A systematic uncertainty of 10 per cent is assumed for $N_{\text{H I}}$. Significantly deviating values, such as the ones for clump D and E of HVC 266.0–18.7+338, are excluded from the calculation. Physical parameters are listed in Table 2.

Venzmer, Kerp & Kalberla (2012) also showed a similar distance gradient using a different approach. Their investigation was based on the velocity structure of three subpopulations in LA I. Future simulations would be useful to assess the likelihood of such a scenario. We note that P/k and n are sensitive to various scenarios as discussed in Section 7.1. The positive Galactic latitude cloud (HVC 297.14+08.5+253) will have a lower n if it is not spherical but twice the size. The trend of n versus Galactic latitude becomes less significant in this case.

In FSM13, the formation of the LA IV remains a mystery. It has a very different morphology than its counterpart (LA I–III). This suggests that LA IV might be formed via a different mechanism or has a different origin. The recent discoveries of ultra-faint dwarf galaxies in the vicinity of the Magellanic System (Bechtol et al. 2015; Drlica-Wagner et al. 2015; Koposov et al. 2015) has renewed theoretical and observational interest (see Westmeier et al. 2015; Yozin & Bekki 2015). The model of Yozin & Bekki (2015) confirms that the locations of these ultra-faint dwarf galaxies are associated with the MCs previously as part of a loose group and shows how they are processed by the Galactic halo upon accretion. This suggests that the clumpy LA IV might be the debris from such an accretion event, which might explain why the three HVCs (part of the LA IV) are further away than the two HVCs near LA I and II. This supports the radial distance estimate of 74 kpc for LA IV in Venzmer et al. (2012).

7.3 Star formation in the leading arm region

Theoretical models and observational evidence show that both the MS and LA were formed via ram-pressure stripping and tidal

interaction between the LMC and SMC (see e.g. Diaz & Bekki 2011; FSM13). Both of these mechanisms are known to trigger star formation in galaxies (e.g. galaxy pair NGC 1512/1510, Koribalski & López-Sánchez 2009 and NGC 4522 in the Virgo cluster, Kenney, van Gorkom & Vollmer 2004). Star formation in the MS and LA has been postulated but there was no success in the hunt for stars being formed *in situ* in early years (e.g. Recillas-Cruz 1982; Guhathakurta & Reitzel 1998). Matthews et al. (2009) conducted a search for star formation in the MS regions using cold atomic gas as an indicator. Two absorption components were identified towards a background radio source, J0119–6809. The corresponding H I column density is $\sim 2 \times 10^{20} \text{ cm}^{-2}$. Follow up observation shows no detection of CO($J=1 \rightarrow 0$) molecular gas associated with the cool gas implying that star formation does not occur at that location within the MS.

Neutral hydrogen gas, dust and molecular hydrogen gas (H_2) act as a reservoir for fuelling star formation activities. This is particularly prominent in high gas density regions. Stars are formed when the dense gas clouds reach the Jeans instability and collapse. Measurements of dust and H_2 are fairly limited in the LA region. An attempt for measuring dust, H_2 and metallicity in the LA has been made by Sembach et al. (2001) on a compact HVC (HVC 287.5+22.5+240). They find that the metallicity of this HVC is similar to the SMC, and the detection of H_2 suggests that either the H_2 formed *in situ* or within the SMC and survived tidal stripping. They prefer the latter scenario given that the formation time-scale of H_2 is long ($\sim 10^8$ yr). If the LA is stripped from the SMC as suggested by simulations (e.g. Diaz & Bekki 2011), we would expect the LA region has a similar H_2 and metallicity content as the SMC, and star formation potentially could occur. In fact, a recent attempt to search for stellar components has been carried out at the optical wavelength by Casetti-Dinescu et al. (2014) in the LA region. Five young stars have been successfully identified and they are believed to have formed in the LA for the first time, using kinematics information, stellar parameters and distance moduli. We examine the location of these five young stars and nearby H I gas content. Four of them are in close proximity of dense clouds with $N_{\text{H I}}$ in the range of 1.5×10^{19} to $1.8 \times 10^{20} \text{ cm}^{-2}$. Clouds with these H I column densities exist everywhere in the LA region and yet the search only resulted in five young stars that were born *in situ*. Where are the missing stars?

The result from Section 7.1 suggests the possibility of different halo environments in the LA region, which might explain the lack of star formation if a special condition is required to form stars. However, without further information on dust and metallicity properties in the entire LA region, it is very hard to assess the conditions that are needed for star formation to occur. The optical search for young stars is currently limited to specific regions. It would be interesting if future optical studies included candidates located in the vicinity of HVC 287.5+22.5+240 to verify if star formation is plausible with the given conditions.

Metallicity and dust might not be the only factors for the star formation in the region. Observational evidence of interaction between the LA I and Galactic disc gas suggests the gas is being compressed by the Galactic halo gas at low z and star formation could also be triggered.

8 SUMMARY

We have studied five HVCs in the vicinity of the Magellanic LA. The targets were selected from the FSM13 catalogue, and high-resolution observations were carried out at the ATCA. We analysed

the combined single-dish GASS and interferometric ATCA data. Clumps were identified and physical parameters were derived for both clumps and diffuse structure of the HVCs. Most of the clumps have a cold component ($\Delta v < 10 \text{ km s}^{-1}$). The unresolved clumps generally consist of a warm component only.

Three of the clouds are part of the LA IV, which lies south of the Galactic plane, and have a head–tail like morphology. The other two are located north the Galactic plane and in close proximity to LA I and LA II. HVC 266.0–18.7+338 is the only cloud that shows a clear velocity gradient. It also consists of many clumps. The V_{LSR} of cold clumps is generally larger than the diffuse (warm) component.

In the case of HVC 276.3–09.0+277, its head is compressed and it does not show any velocity gradient. The velocity of the cold component decreases gradually and is larger than that of warm component. Two clumps are located in the two main cores of the cloud. The third clump is relatively small and unresolved. It is located slightly offset from one of the clumps.

HVC 297.1+08.5+253 has been studied by [BBKW06](#). They analysed the single-dish and interferometer data separately. Their analysis focuses on the core of the head–tail structure and many clumps have been identified. We, on the other hand, carried out the analysis by using the combined image. This allows us to probe large- and small-scale structures simultaneously. In our analysis, the N_{HI} increases towards the head of the cloud and decreases afterward. The cold component shows the same N_{HI} pattern except that it peaks at a slightly different position from the warm component. There is a small velocity gradient at the tail of the cloud. Otherwise, velocity is constant for both cold and warm components.

The analysis of the combined image of HVC 310.3+08.1+167 was carried out on a smoothed cube due to it being very diffuse and low in surface brightness. It consists of many clumps, and all of them are unresolved with cold components. Overall, the velocity linewidth of both the cold and warm components follows the same trend as the N_{HI} .

We discussed the HVC phase diagram ($\log P/k$ versus $\log n$) using the model of [Wolfire et al. \(1995\)](#). The model has metallicity and gas-to-dust ratio of 0.3, which is based on the assumption that the gas was stripped from the LMC. All the clouds are in the instability valley where they can maintain their two-phase structures. Interestingly, there is an offset between the data points and their corresponding height above the Galactic plane. A lower metallicity model is a better fit for the majority of the data points, which suggests that the gas was likely stripped from the SMC. This is consistent with various simulations (e.g. [Diaz & Bekki 2011](#)). We find a gradient in thermal halo pressure, hydrogen density and H I column density as a function of Galactic latitude. This is the first possible observational evidence of an increasing Galactocentric distance from the trailing end to the leading part of the LA, although further observations may be needed to confirm. A different halo environment might explain the low star formation rate in the LA region. Special conditions such as additional dust and atomic hydrogen gas are needed in order to trigger star formation. Future studies of the atomic hydrogen gas content in the region and the search for more stars will be important to understand the star formation history in the region of the LA.

ACKNOWLEDGEMENTS

B-QF was the recipient of a John Stocker Postdoctoral Fellowship from the Science and Industry Research Fund. NMc-G acknowledges CSIRO Astronomy & Space Science where this work was commenced. This publication made use of data products from

the Parkes and ATCA radio telescopes. The Australia Telescope Compact Array/Parkes radio telescope is part of the Australia Telescope National Facility, which is funded by the Commonwealth of Australia for operation as a National Facility managed by CSIRO.

REFERENCES

- Bechtol K. et al., 2015, *ApJ*, 807, 50
 Ben Bekhti N., Brüns C., Kerp J., Westmeier T., 2006, *A&A*, 457, 917 (BBKW06)
 Blitz L., Spergel D. N., Teuben P. J., Hartmann D., Burton W. B., 1999, *ApJ*, 514, 818
 Braun R., Burton W. B., 1999, *A&A*, 341, 437
 Brüns C., Westmeier T., 2004, *A&A*, 426, L9
 Brüns C., Kerp J., Kalberla P. M. W., Mebold U., 2000, *A&A*, 357, 120
 Brüns C., Kerp J., Pagels A., 2001, *A&A*, 370, L26
 Brüns C. et al., 2005, *A&A*, 432, 45
 Casetti-Dinescu D. I., Moni Bidin C., Girard T. M., Méndez R. A., Vieira K., Korchagin V. I., van Alena W. F., 2014, *ApJ*, 784, L37
 Diaz J., Bekki K., 2011, *MNRAS*, 413, 2015
 Drlica-Wagner A. et al., 2015, *ApJ*, 813, 109
 For B.-Q., Staveley-Smith L., McClure-Griffiths N. M., 2013, *ApJ*, 764, 74 (FSM13)
 For B.-Q., Staveley-Smith L., Matthews D., McClure-Griffiths N. M., 2014, *ApJ*, 792, 43
 Guhathakurta P., Reitzel D. B., 1998, in *Zaritsky D., ed., Astronomical Society of the Pacific Conference Series Vol. 136, Galactic Haloes*. Astron. Soc. Pac., San Francisco, p. 22
 Hartmann D., Burton W. B., 1997, *Atlas of Galactic Neutral Hydrogen*. Cambridge University Press, Cambridge
 Kalberla P. M. W. et al., 2010, *A&A*, 521, A17
 Kenney J. D. P., van Gorkom J. H., Vollmer B., 2004, *AJ*, 127, 3361
 Klypin A., Kravtsov A. V., Valenzuela O., Prada F., 1999, *ApJ*, 522, 82
 Kopusov S. E., Belokurov V., Torrealba G., Evans N. W., 2015, *ApJ*, 805, 130
 Koribalski B. S., López-Sánchez Á. R., 2009, *MNRAS*, 400, 1749
 Mathewson D. S., Cleary M. N., Murray J. D., 1974, *ApJ*, 190, 291
 Matthews D., Staveley-Smith L., Dyson P., Muller E., 2009, *ApJ*, 691, L115
 McClure-Griffiths N. M. et al., 2008, *ApJ*, 673, L143
 McClure-Griffiths N. M. et al., 2009, *ApJS*, 181, 398
 Moore B., Ghigna S., Governato F., Lake G., Quinn T., Stadel J., Tozzi P., 1999, *ApJ*, 524, L19
 Muller C. A., Oort J. H., Raimond E., 1963, *Academie des Sciences Paris Comptes Rendus*, 257, 1661
 Pietrzyński G. et al., 2013, *Nature*, 495, 76
 Pisano D. J., Barnes D. G., Gibson B. K., Staveley-Smith L., Freeman K. C., Kilborn V. A., 2004, *ApJ*, 610, L17
 Putman M. E., Saul D. R., Mets E., 2011, *MNRAS*, 418, 1575
 Recillas-Cruz E., 1982, *MNRAS*, 201, 473
 Salem M., Besla G., Bryan G., Putman M., van der Marel R. P., Tonnesen S., 2015, *ApJ*, 815, 77
 Sault R. J., Teuben P. J., Wright M. C. H., 1995, in *Shaw R. A., Payne H. E., Hayes J. J. E., eds, Astronomical Society of the Pacific Conference Series Vol. 77, Astronomical Data Analysis Software and Systems IV*. Astron. Soc. Pac., San Francisco, p. 433
 Sembach K. R., Howk J. C., Savage B. D., Shull J. M., 2001, *AJ*, 121, 992
 Stanimirović S., 2002, in *Stanimirović S., Altschuler D., Goldsmith P., Salter C., eds, Astronomical Society of the Pacific Conference Series Vol. 278, Single-Dish Radio Astronomy: Techniques and Applications*. Astron. Soc. Pac., San Francisco, p. 375
 Stanimirović S., Hoffman S., Heiles C., Douglas K. A., Putman M., Peek J. E. G., 2008, *ApJ*, 680, 276
 Steer D. G., Dewdney P. E., Ito M. R., 1984, *A&A*, 137, 159

Venzmer M. S., Kerp J., Kalberla P. M. W., 2012, *A&A*, 547, A12
Wakker B. P., 1991, *A&A*, 250, 499
Westmeier T., Brüns C., Kerp J., 2005, *A&A*, 432, 937
Westmeier T., Staveley-Smith L., Calabretta M., Jurek R., Koribalski B. S.,
Meyer M., Popping A., Wong O. I., 2015, *MNRAS*, 453, 338
Williams J. P., de Geus E. J., Blitz L., 1994, *ApJ*, 428, 693
Wilson W. E. et al., 2011, *MNRAS*, 416, 832

Wolfire M. G., McKee C. F., Hollenbach D., Tielens A. G. G. M., 1995,
ApJ, 453, 673
Yozin C., Bekki K., 2015, *MNRAS*, 453, 2302
Zwaan M. A., 2001, *MNRAS*, 325, 1142

This paper has been typeset from a \TeX/L\AA\TeX file prepared by the author.